Combining the Converse Humidity/Resistance Response Behaviors of RGO Films for Flexible Logic Devices

Journal of Materials Chemistry C

Accepted Manuscript

This article can be cited before page numbers have been issued, to do this please use: Y. Tai, T. Kanti Bera, G. Lubineau and Z. Yang, *J. Mater. Chem. C*, 2017, DOI: 10.1039/C7TC00686A.

ROYAL SOCIETY OF CHEMISTRY

rsc.li/materials-c

View Article Online
DOI: 10.1039/C7TC00686A

Journal Name

ARTICLE

Combining the Converse Humidity/Resistance Response Behaviors of RGO Films for Flexible Logic Devices

Received 00th January 20xx,
Accepted 00th January 20xx

DOI: 10.1039/x0xx00000x

www.rsc.org/

Yanlong Tai,[1,2] Tushar Kanti Bera,[2] Gilles Lubineau,*[2] Zhenguo Yang*[1]

Carbon nanomaterials have excellent humidity sensing performance. Here, we demonstrate that reduced-graphene-oxide-(rGO) based conductive films with different thermal reduction times have gradient and invertible humidity/electrical resistance responses: rGO films (< 11 h, negative response, regarded as a signal of "0"), rGO films (around 11-13 h, balance point) and rGO films (> 13 h, negative response, regarded as a signal of "1"). We propose a new mechanism that describes a "scale"-like model for rGO films to explain these behaviors based on contributions from Ohm-contact resistance and capacitive reactance at interplate junctions, and intrinsic resistances of the nanoplates, respectively. This mechanism is accordingly validated via a series of experiments and electrical impedance spectroscopies, which complement more classical models based on proton conductivity. To explore the practical applications of the converse humidity/resistance responses, three simple flexible logic devices were developed, i) a rGO pattern for humidity-insensitive conductive film, which has the potential to greatly improve the stability of carbon-based electrical device to humidity; ii) a Janus pattern of rGO films for gesture recognition, which is very useful to human/machine interactions; iii) a sandwich pattern of rGO films for 3-dimensional (3D) noncontact sensing, which will be complementary to existing 3D touch technique.

Introduction

Carbon-nanomaterials-based humidity sensors (carbon nanotubes, CNTs and reduced graphene oxide, rGO) are attracting more attention in recent years owing to their excellent humidity-sensing capability,[1-3] which also have been extensively applied to semiconductor manufacturing,[4] packaging industry,[5] pharmaceutical and food processing,[6,7] electronic processing,[8] etc.. Compared with traditional humidity sensing materials, like ceramics (e.g., Al_2O_3 and Si_3N_4),[9,10] metal oxides (e.g., SnO_2, and GaN)[11,12] and polymers (e.g., polyelectrolytes and conducting polymers),[13,14] carbon-based nanomaterials usually exhibit larger surface-to-volume ratio, faster response, higher mechanical and chemical stability, lower cost, and suitability for large-scale manufacture and deployment.[15,16]

The humidity-sensing mechanisms of carbon nanomaterials were also investigated via theoretical calculations and experimental demonstrations.[17,18] Based on the generally accepted explanation of protonic conduction model, their sensing behaviours are strong related to the hydrophilic functional groups (e.g., epoxy, hydroxyl, and carboxyl), which can absorb or desorb water molecules in the environment with high efficiency through physical diffusion or hydrogen bonding.[19,20] The absorbed water molecules can produce hydronium ions (H_3O^+) as charge carriers through an ionized process when an electrostatic field is applied to the carbon nanomaterials.[21] Experimental results show that water molecules are observed to increase the electrical conductivity of n-type nanomaterials and to decrease the electrical conductivity of p-type nanomaterials.[22,23] Although CNTs behave similarly to p-type nanomaterials and rGOs behave similarly to n-type nanomaterials in terms of their resistance response to humidity,[24,25] we cannot simply conclude that these materials should be grouped accordingly.[26,27] Categorization of these materials requires that we also consider the microstructure of each material. This type of investigation will further clarify how water molecules affect the resistance response and ultimately the electrical conductivity of these materials.

Here, to exactly explain the opposite humidity/resistance response of CNT and rGO to humidity stimulus, meanwhile avoiding the influence from the differences in microstructures, rGO films with different thermal reduction times were employed, as well as explore their promising applications.

[1]Fudan University, Department of Materials Science, Shanghai 200433, China
*Email: zqyang@fudan.edu.cn (Prof. Zhenguo Yang)
[2]King Abdullah University of Science and Technology (KAUST), Physical Sciences and Engineering Division, COHMAS Laboratory, Thuwal 23955-6900, Saudi Arabia.
*E-mail: gilles.lubineau@kaust.edu.sa (Prof. Gilles Lubineau)

†Electronic Supplementary Information (ESI) available: [details of any supplementary information available should be included here]. See DOI: 10.1039/x0xx00000x

View Article Online
DOI: 10.1039/C7TC00686A

First, a "scale"-like model was introduced to describe the microstructure of rGO film, combining the changes in intrinsic resistance of the plates and junction resistance between the plates (Figure 1a). Then, a gradient and investible humidity/resistance response of rGO films with different thermal reduction times under identical conditions was presented: rGO with less reduction time decrease their resistance (negative response), that with more reduction time increase their resistance (positive response, like that of CNTs), as well as a balance point showing a humidity-insensitive performance.

Second, we experimentally investigated the gradient change of physical/chemical performance of rGO films with different thermal reduction times, and explained the invertible behavior through the contribution from ohm-contact resistance and capacitive reactance at interplate junctions, and intrinsic resistances of the nanoplates, respectively, based on electrical impedance spectroscopy.

Third, we explore how the gradient and invertible humidity/resistance response of rGO films with different thermal-reduction times can be applied to flexible logic devices via simple logic-pattern designs (negative response defined as"0" and positive response as "1"), incl. i) a type of humidity-insensitive rGO film close to "zero"-resistance rlative change independent of changing humidity (defined at ± 0.3 %); ii) a Janus pattern of rGO films (positive-negative) for egesture recognition; iii) a sandwich pattern of rGO films (positive-negative-positive or negative-positive-negative) for 3-dimensional (3D) noncontact sensing technique.

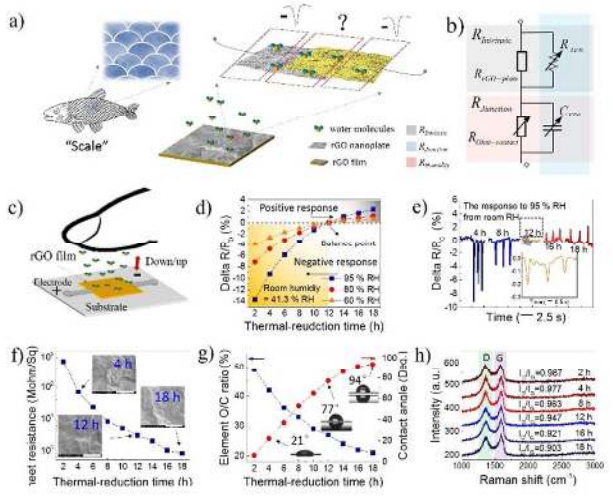

Figure 1. Electrical resistance responses to humidity and physical performance of rGO films with different thermal reduction times. a) Scale microstructural model for rGO films, and b) the equivalent electrical circuitry model representing intrinsic and junction-dependent resistance responses ($R_{Intrinsic}$ and $R_{Junction}$: intrinsic resistance and resistance at junction of rGO; R_{Ion} and C_{EDL}: contribution of resistance change from environmental humidity). c) The measurement illustration used to investigate the humidity/resistance response; A human-index finger is the source of humidity; The size of carbon film is 10 × 10 mm. d) The gradient and invertible humidity/resistance response of rGO films with different thermal reduction times, incl. negative response, positive response and balance point (the defined standard: resistance variation: ± 0.3 %), and e) the corresponding cyclic performance; Inset in e) is the enlarged image of the balance point; The test frequency is around 1 Hz. The gradient physical/chemical performance: f) sheet resistance, g) element oxygen (O)/carbon(C) ratio and contact angle, h) Raman spectrums of rGO films with different thermal reduction times; Insets in f) are SEM images of rGO films with the scale bar of 1 μm. Insets in g) are the digital images of contact angles. Note that the room humidity is 41.3 % RH, the default thermal-reduction temperature is 150 ℃, and every data point is the average value from three samples.

Results and discussion

To exactly explain why CNT and rGO films have a converse resistance response to humidity stimulus, rGO films were employed because of their tunable physical/chemical performance via different thermal reduction times. In specific, with the longer thermal reduction time, its physical/chemical performance (hydrophobicity, conductivity, etc.) is close to that of CNT films.[28] More important, the differences in microstructures between CNT and rGO films (bulk density, junction amount, etc.) also can be avoided effectively.

Accordingly, a "scale"-like model was introduced to describe the microstructure of rGO film, which can be confirmed through the scanning electron microscopy (SEM) of rGO film in Figure 1a. Thus, total macroscopic resistance of rGO films is mainly composed of the intrinsic resistance of the nanoplate ($R_{Intrinsic}$) and the junction resistance between nanoplates ($R_{Junction}$, $R_{Junction} > R_{Intrinsic}$).[29,30]

As moisture absorption increases, each film responds with a different resistance. The intrinsic-resistance response involves the formation of hydronium ions (H_3O^+), which behave as charge carriers that tend to decrease the intrinsic resistance (negative response), indicating its weaker influence to the macroscopic resistance of rGO film. Resistance at junctions involves the intercalation of water molecules at the interface between nanoplates, which not only increases the interplate distance due to the humidity expansion of rGO film, but also causes a switch from ohmic-type to ohmic/capacitive-type behavior.[31] According to Ohm law, the increased distance leads to the increase of ohm-contact resistance, whereas the generated capacitive contact (electrical double layer, C_{EDL}) induced the decrease of $R_{Junction}$ due to its parallel connection to ohm-contact resistance.[32] Thus, the final response behavior of $R_{Junction}$ is the balanced results of $R_{ohm\text{-}contact}$ (thermal-reduction time and humidity dependent) and CEDL (humidity dependent). Besides, these are represented schematically by the equivalent electrical circuit shown in Figure 1b.

Gradient response in resistance to humidity

To explain the above issue, we fabricated rGO-based conductive patterns (10 × 10 mm) of each with comparable thicknesses (26 ± 3

View Article Online
DOI: 10.1039/C7TC00686A

nm) on polyethylene terephthalate (PET) substrates (Figure S1). Humidity was controlled by adjusting the distance between the finger and the conductive film, as seen in Figure 1c.

Figure 1d summarized the relative resistance change of rGO films with different thermal-reduction times to humidity (Delta $R/R_0 = (R_1 - R_0)/R_0$, where R_0 and R_1 are the original and updated resistance, respectively). In specific, with the increase of thermal-reduction time at 150 ℃ and the relative humidity changing from 41.3 % to 95 %, the negative change in resistance of GO films (around -13.7 % for 2 h) reached zero for around 12 h, then switched to a positive resistance response (2.4 % for 18 h). Similar phenomena also can be observed at other humidity changes from 41.3% to 60 %, to 80 %, respectively. Moreover, the corresponding cyclic-response curves were shown in Figure 1e to confirm the stability of humidity sensing capability of rGO films. It can be seen that the resistance change at balance point is only about 0.18 % when the relative humidity changes from 41.3 % to 95 %, which meets the humidity-insensitive standard within 0.3 % we defined here.

To reveal what has happened, the physical/chemical performance of rGO films with different thermal-reduction times was monitored. Results in Figure 1f show that the sheet resistance of rGO films decreased from 69 Mohm (4 h) to 3 Mohm (12 h) to 0.8 Mohm (18 h) though we almost can't found any change in microstructure (inset SEM images of Figure 1f). Meanwhile, the O:C ratio decreased from 42.3 (4 h) to 27 (12 h) to 21 (18 h), compared with the DI-water based contact angle from 22 ° (4 h) to 77 ° (12 h) to 94 ° (18 h), respectively, as seen in Figure 1g and Figure S2. Moreover, we also observed the gradient variation of the intensity- D/G ratio (I_D/I_G) in their Raman plots in Figure 1h, which presented a lower value in rGO film that underwent a longer reduction time from 0.977 (4 h) to 0.947 (12 h) to 0.903 (18 h), respectively, indicating the increase of purity and decrease of defect of rGO films. According to previous reports, these gradient changes have to contribute to the gradual decrease of the number of hydrophilic functional groups (e.g., epoxy, hydroxyl and carboxyl) on the surface of rGO particles via the detachment of water molecules, along with the number of defects during the reduction process.

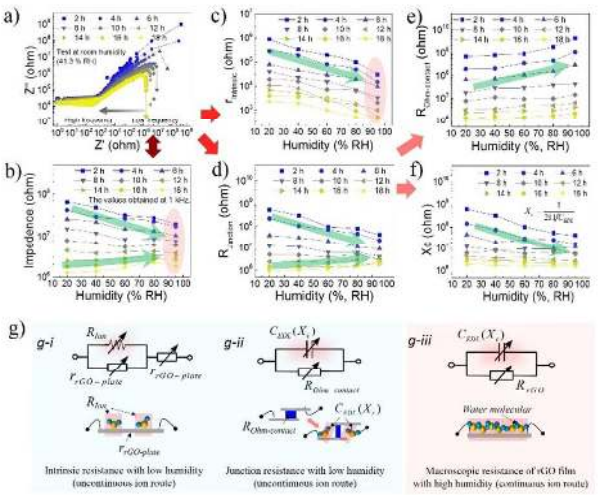

Figure 2. Theoretical analysis of invertible humidity/resistance response via electrical impedance spectroscopy (EIS). a) Electrical impedance spectroscopies and b) Humidity/impedance response of rGO films with different thermal-reduction times; The default room humidity of 41.3 % RH, and the test frequency is 1 kHz. The resistance behavior in response to humidity of the components in the equivalent circuit models (Figure 1b): c) $R_{Intrinsic}$; e) $R_{Junction}$; f) $R_{Ohm\text{-}contact}$ and Xc (CEDL depended, calculated via the equation of $X_C = 1/(2\pi f C_{EDL})$) at junctions; respectively. g) The possible equivalent circuit models of rGO films suffered by humidity stimulus generated via a MATLAB-based impedance curve fitting program: g-i, intrinsic resistance and g-ii, junction resistance of rGO film with low humidity (uncontinous ion route), g-iii, macroscopic resistance of rGO film with high humidity (continuous ion route), respectively, as well as the corresponding mechanism illustrations of various resistance variations. The red arrows is used to show the logic relationship from a) to f). The green arrows in from b) to f) is used to show the trend of resistance change to different humidities and thermal-reduction times. The red area in b) and c) shows the influence from a high humidity environment. The default sample size was 10 × 10 mm fabricated using an ink concentration of 0.1 mg/ml. Room RH was 41.3 % and room temperature was 25.2 ℃. Every data point is the average value from three samples.

Invertible response in resistance to humidity

To address the invertible humidity/resistance response behavior, the relative contributions of $R_{Intrinsic}$, $R_{ohm\text{-}contact}$ and C_{EDL} at junction of rGO film were analyzed via electrical impedance spectroscopy (EIS), as seen in Figure 2a to 2f. The corresponding equivalent circuits were generated via a MATLAB-based impedance curve fitting program (S1 and Figure 2g).[33-35]

Figure 2a and S3 presented the EIS plots of rGO films with different thermal-reduction times at different environmental , 20 %, 41.3 %, 60 %, 80 %, and 95 %, RH, respectively. Results show that, with the increase of thermal-reduction time, both the real and the imaginary parts of the resistance decreased, indicating the electrical improvement of rGO via thermal reduction. Whereas, to demonstrate the responding differences of each film, the impedance values at 1 kHz were collected and plotted, as seen in Figure 2b. In specific, when the thermal-reduction time below 11 h, the impedance of rGO films decreased with the increased humidity, showing a negative response. On the contrary, when the thermal-reduction time above 13 h, the impedance of rGO films increased with the increased humidity, showing a positive response. Within 11-13 h of the thermal-reduction time, the impedance of rGO films is close to stable, showing the humidity-insensitive performance. These gradient and invertible response behaviors are high consistent with what we have got in Figure 1d and 1e. Accordingly, the possible equivalent circuit models of rGO films suffered by humidity stimulus in Figure 1b was further revealed via a MATLAB-based impedance curve fitting program, as well as the corresponding mechanism illustrations of resistance variation, as seen in Figure 2g. The excellent fitting results in Figure S4 indicate the efficiency of this strategy.

When humidity is low (e.g. < 85 % RH), the generated hydronium ions (H_3O^+) can't form a continuous conductive route. As for $R_{Intrinsic}$, only partial area of rGO nanoplates ($R_{rGO\text{-}plate}$) was influenced by

View Article Online
DOI: 10.1039/C7TC00686A

H_3O^+ (R_{Ion}), as illustrated in g-i. Due to the parallel connection between $R_{rGO\text{-}plate}$ and R_{Ion}, humidity always makes $R_{Intrinsic}$ decrease. This prediction can be confirmed in Figure 2c. As for $R_{Junction}$, this influence from humidity is more complex, as seen in g-ii. On one side, the generated R_{Ion} forms C_{EDL} between graphene nanoplates, which is parallel connected with the original $R_{Ohm\text{-}connect}$. Similarly, this influence will lead to the decrease of $R_{Junction}$; On the other side, the absorption of water molecules will make the increase of distance between rGO nanoplates due to expansion of rGO films. The reduction of contact area will result in the increase of $R_{Ohm\text{-}connect}$ according to Ohm law. Therefore, the final change trend of resistance at junctions is the combined results. Figure 2d present the change of role intuitively, similar like that in Figure 1d, 1e and 2b.

Consequently, compared with the data in Figure 2c and 2d, it also can be found that is $R_{Junction}$ (10^5 - 10^9 ohm) always lager than $R_{Intrinsic}$ (10^3 - 10^7 ohm), around 100 times for the same rGO film. This is consistent with our previous report that $R_{Junction}$ plays a crucial role in a nanomaterial-based conductive film. Therefore, the humidity response of $R_{Junction}$ was further revealed via the contribution of both $R_{Ohm\text{-}connect}$ and C_{EDL}. As for $R_{Ohm\text{-}connect}$, it is proportional to environmental humidity, and inversely proportional to thermal-reduction time, as analyzed above and verified in Figure 2e. As for C_{EDL}, it's influence can be presented via capacitive reactance (Xc, $Xc=1/(2\pi fC_{EDL})$),[36] as seen in S1 and Figure 2f, which presented a jus opposite proportional relationship to environmental humidity, and a similar proportional relationship to thermal-reduction time, compared with $R_{Ohm\text{-}connect}$.

However, we found that, as for rGO films with less thermal-reduction time (< 10 h), the value of Xc is lower than $R_{Ohm\text{-}connect}$, which means that $R_{Junction}$ is close to demonstrate the response behavior of Xc to humidity due to their parallel connection, negative response. With more thermal-reduction time (< 13 h), $R_{Ohm\text{-}connect}$ decrease quickly due to the improved macroscopic electrical resistance of rGO film. Whereas, Xc is relative stable, which is mainly humidity dependent, as well as the decrease of functional groups on rGO nanoplate, which can generate ions to form C_{EDL}. Therefore, $R_{Ohm\text{-}connect}$ is lower than Xc, determining the response behavior of $R_{Junction}$, positive response. Between 11-13 h, the variation of both $R_{Ohm\text{-}connect}$ and Xc reached a balance point, showing humidity-insensitive performance. This mechanism can well explain phenomena in Figure 2b and 2d well.

When humidity is high (e.g. > 85 % RH), a continuous ion path can forms, which is parallel connected with rGO film and cause the decrease of macroscopic electrical resistance of rGO film.[37] The corresponding equivalent circuit model can be seen in figure 2g-iii. This is can be used to explain why the original increase trend of resistance start to decrease, as seen in Figure 2b and 2c. This phenomenon also have been reported before, and only explained that the carbon materials have transferred from p-type to n-type semiconductor.[38]

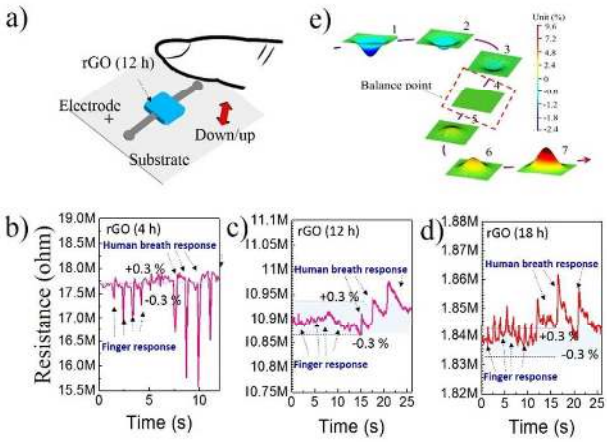

Figure 3. Humidity-insensitive performance of rGO films. a) Illustraton and b)-d) real-time humidity-resistance response curves of rGO film (4 h, 12 h, 18 h, respectively) to a down/up motion of a human-index finger and human breath; The ± 0.3 % in b), c) and d) is the defined standard for humidity-insensitive materials. e) 3D illustration of the mapped change in resistance across the noncontact sensing logic devices based on a Gaussian function: rGO films with different thermal-reduction times (1, 4 h; 2, 8 h; 3,10 h; 4, 12 h; 5, 14 h; 6, 16 h; 7, 18 h; respectively) with the balance scope (11-13 h); Note that the positive resistance change represented by a convex peak and the negative resistance change represented by a concave peak. The default moving speed of human-index finger is: 1.8 s/period.

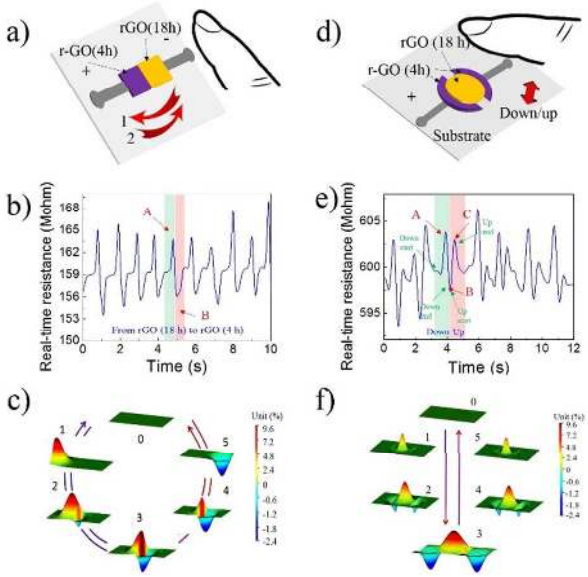

Figure 4. Transparent, flexible noncontact-sensing logic devices. a) Illustration and b) real-time resistance response to gesture recognition from rGO (18 h) to rGO (4 h) with a fixed distance of 3 mm between human-index finger and rGO film. c) Illustration and d) real-time resistance response of a 3D noncontact-sensing technique

View Article Online
DOI: 10.1039/C7TC00686A

through a down/up period test of a human-index finger from 10 mm to 1 mm. 3D illustration of the mapped change in resistance across the noncontact sensing logic devices based on a Gaussian function: c) gesture recognition from 0-2-4-0; i) 3D noncontact-sensing technique from 0-1-3-5-0; respectively. Note that the positive resistance change represented by a convex peak and the negative resistance change represented by a concave peak. The default moving speed of human-index finger is: 1.8 s/period.

Application to flexible logic devices

Humidity-insensitive performance

We constructed one humidity-insensitive rGO-based conductive film (10 × 10 mm) through adjusting its thermal-reduction time. The mechanism of this performance is the balanced results of Ohm-contact resistance and capacitive-contact reactance to humidity stimulus at the junctions of rGO film, as addressed above. Our objective was to achieve near-zero relative change in resistance (delta R/R_0) independent of changing humidity, which we define as less than 0.3 %.

A rGO-based conductive film reduced at 150 ℃ for 12 h were chosen for demonstration with a sheet resistance of 4.2 ± 0.5 Mohm/sq, a transmittance of 87 % and its microstructure in Figure 1f and S1. This humidity-insensitive performance was verified through its real-time resistance response to human-index finger and breath, respectively (Figure 3a and 3b). It can be found that, compared with rGO films with 4 h and 18 h in Figure 3a and 3c, the variations in resistance of rGO (12 h, Figure 3b) to human finger and breath are within the range of ± 0.3 % of its original resistance, which meet the condition of humidity insensitive materials we defined above. Besides, this performance is further demonstrated by the 3D illustration based on a Gaussian function in Figure 3c.[39] More details can refer to Video-1#, -2# and -3#.

Gesture recognition

Two films (sample size is 10 × 5 mm, 1/2 length for rGO (4 h), 1/2 length for rGO (18 h)) were combined on a PET substrate (Figure 3d) to create a gesture recognition device by exploiting the opposite resistance responses of both rGO films to humidity.[40] This transparent flexible logic device is presented in Figure S5a and 5b, and their microstructure can be seen in Figure S6.

The efficiency of the device was confirmed, as shown in Figure 3e and Video-4#, by moving a human-index finger from rGO (18 h) to rGO (4 h) to generate first a positive resistance response (defined as peak-A) followed by negative resistance response (defined as peak-B), and vice versa. The final relative change in resistance at each time point is the combined result of the resistance response to humidity of each film; this is further demonstrated by the 3D illustration based on a Gaussian function in Figure 3f. The real-time resistance-change profile shows that response periods were always less than 1 s, a completely acceptable rate for practical applications. The subsequent transparent, flexible device can recognize human-finger gestures in a noncontact mode effectively.

3D noncontact-sensing technique

A transparent flexible pattern of equal sections of rGO (18 h) sandwiched a section of rGO (4 h) (rGO (4 h)/rGO(18 h)/rGO(4 h)) was fabricated on an 10 × 5 mm PET substrate (Figure 3g, S5c and S5d). Here, our objective was to determine whether this system would be suitable for 3D noncontact sensing.[41-43] Because fingertips have a spherical shape, humidity is not introduced uniformly over the area covered by the three conductive films. Thus, when the human-index finger approaches the connected rGO (4 h)/rGO(18 h)/rGO(4 h) film, the rGO (18 h) portion of the film will sense its humidity before the rGO (4 h) portion of the film. Thus, when the finger approaches the center of the system, a positive resistance response will first be generated by the rGO (18 h) portion of the film, defined as peak-A, followed by a negative resistance response generated by the rGO (4 h) portion of the film. When the combination of these two changes in resistance cancel each other out, resistance reaches zero, and if the resistance from the rGO (4 h) becomes stronger, resistance reaches the negative zone, defined as peak-B. As the finger is slowly removed, resistance immediately returns toward the positive zone, indicating stronger resistance from the rGO (18 h), defined as peak-C. Therefore, each introduction and removal of the finger (finger displacement) causes three peaks (two positive and one negative) that correspond to three signals.

Figure 3h shows that the profile is very regular from one cycle to the next, with similar positive/negative peak values and response times for each period (approximately 1.4 s). Consistency in response time demonstrates that results have great repeatability and stability. For a single-period profile, three peaks (two positive peaks and one negative peak) are clearly identifiable. A single-period profile is further demonstrated via 3D illustration based on a Gaussian function in Figure 3i. More details can refer to Video-5#.

Conclusions

We demonstrate a phenomenon that a gradient, invertible humidity/electrical resistance responses of rGO based conductive films, which can be controlled via different thermal-reduction times: rGO film (<11 h, negative response, regarded as a signal of "0"), rGO film (around 11-13 h, balance point) and rGO film (>13 h, negative response, regarded as a signal of "1"). We propose a new mechanism with a "scale"-like model for rGO films to explain these behaviors, and verify it accordingly through electrical impedance spectroscopies, which complement more classical models based on proton conductivity. We explore three kinds of flexible logic devices, incl. a rGO pattern for humidity-insensitive conductive film, a Janus pattern of rGO films for gesture recognition, and a sandwich pattern of rGO films for 3-dimensional (3D) noncontact sensing, which will be complementary to existing 3D touch technique. Further investigations are necessary to explore more avenues for their applications to flexible logic devices, as well as other potential materials.

Experimental

Materials

View Article Online
DOI: 10.1039/C7TC00686A

Graphene oxide ink (0.1 mg/ml) was prepared in the lab from purified natural graphite (SP-1, Bay Carbon) by the Hummers method with the plate diameter of 0.2-1.5 µm, as shown in Figure S1. [31] Polyethylene terephthalate (PET) films were purchased from Teonex® Inc. with a thickness of 125 µm. DI water was used in all experimental processes.

Fabrication of rGO-based flexible logic devices

RGO-based conductive films were prepared by drop casting on a PET substrate. Specifically, PET films were treated with oxygen plasma at 100 W for 60 s to improve the hydrophilicity of the substrate. Next, the as-prepared inks were dropped onto a rectangular Teflon frame (10 × 10 mm) using a Thermo Scientific Finnpipette (0.2 - 2 µl) with a controlled surface concentration of 1 µl/cm2. Before the Teflon frame was peeled off, this ink were baked on an oven at 150 ℃ for 2 h, defined as sample-1; for 4 h, defined as sample-2; for 6 h, defined as sample-3, and so on. The entire process was performed gently to achieve a homogeneous film.

RGO-based Janus pattern with the size of 10 × 5 mm (1/2 length for rGO (4 h), 1/2 length for rGO (18 h)) was fabricated step by step according to above method. In specific, the pattern of rGO (18 h) was deposited on PET substrate first via a rectangular Teflon frame (5 × 5 mm). After baked at 150 ℃ for 14 h, the other rGO pattern (5 × 5 mm) was deposited accordingly, then baked another 4 h.

RGO-based sandwich pattern with the size of 10 × 5 mm (1/3 for rGO (4 h), 1/3 for rGO (18 h), 1/3 for rGO (4 h), respectively) was also fabricated was fabricated on PET substrate step by step according to above method.

Typical rGO-based conductive film, Janus pattern and sandwich pattern are shown in Figure S5.

Characterization and measurements

The surface microstructure of the prepared rGO-based conductive films was examined by SEM (Quanta 600, FEI Company) and by profilometry (Veeco Dektak 150 operating at a scanning speed of 0.167 µm/s). Energy-dispersive X-ray spectroscopy (EDS) was performed for surface elemental analysis using an EDS detector operating at 20 kV. Static contact angle measurements (VCA video contact angle system, AST Products, Billerica, MA) of DI water were performed using the sessile drop method to evaluate surface wettability. Raman spectra of the surface of MWCNT and GO were collected using a LabRAM Aramis Raman spectrometer (Horiba, Ltd.) on casted films using a 473-nm laser for structural analysis. 4-point probe system (Pro4-440N, Lucas Labs) was used to monitor the change of sheet resistance. An LCR meter (E4982A, Agilent Technologies) was used with frequencies ranging from 20 Hz to 2 MHz to measure electrical impedance spectroscopies under different environmental humilities, assisted through calculation and a MATLAB-based impedance curve fitting program, as seen in Figure S7. A multimeter (Agilent 34401A) that allowed data to be recorded on a PC was used to map the real-time resistance response to humidity. A climatic chamber (Tenney, T2RC, Thermal Product Solutions) was used to provide the stable environment with a desired humidity and temperature.

Note that a human-index finger was used as the humidity source. To ensure precise control of the environmental conditions, humidity and temperature around the finger were thoroughly mapped using a humidity meter (TM325, Dickson), as shown in the inset of Figure S8. Environmental humidity was defined according to the distance (using a ruler) between the index finger and the sample. This method is effective for verifying the efficiency of these devices intuitively in practical applications of human-finger electronics. The default room relative humidity and temperature were 41.3 % and 25.2 ℃, respectively.

Acknowledgements

We express gratitude to the key discipline fund of Shanghai (B117) for financial support and AKM Industrial Ltd for helpful discussions. This work was also partially supported by Baseline Funding from King Abdullah University of Science and Technology (KAUST).

References

1. J. J. Boland, *Nat*. *Mater*. **2010**, 9, 790-792.
2. D. R. Dreyer, S. Park, , C. W. Bielawski, R. S., Ruoff, *Chem. Soc. Rev.* **2010**, 39, 228-240.
3. G. Peng, S. Wu, J. E. Ellis, X. Xu, G. Xu, C. Yu, A. Star, *J. Mater. Chem. C* **2016**, 4, 6575-6580.
4. Y. Liu, J. Parisi, X. Sun, Y. Lei, *J. Mater. Chem. A* **2014**, 2, 9919-9943.
5. Y. Feng, L. Xie, Q. Chen, L. R. Zheng, *IEEE Sens. J.* **2015**, *15*, 3201-3208.
6. V. Andronis, G. Zografi, *Pharm. Res.* 19**8**8, *15*, 835-842.
7. F. Bibi, C. Guillaume, A. Vena, N. Gontard, B. Sorli, *Sensor. Actuat. A-Phys.* **2016**, *247*, 355-367.
8. C. Melios, A. Centeno, A. Zurutuza, V. Panchal, C. E. Giusca, S. Spencer, O. Kazakova, *Carbon* **2016**, *103*, 273-280.
9. C. Pacholski, A. Kornowski, H. Weller, *Angew. Chem. Int. Edit*. **2002**, 41, 1188-1194.
10. A. I. Buvailo, Y. Xing, J. Hines, N. Dollahon, E. Borguet, A*CS Appl. Mater. Inter.* **2011**, 3. 528-533.
11. P. Sahoo, D. S. Oliveira, M. A. Cotta, S. Dhara, S. Dash, A. K. Tyagi, B. Raj, *J. Phys. Chem*. C **2011**, 115, 5863-5867.
12. Q. Kuang, C. Lao, Z. L. Wang, Z. Xie, L. Zheng, *J. Am. Chem. Soc*. **2007**, 129, 6070-6071.
13. L. T. de Haan, J. M. Verjans, D. J. Broer, C. W. Bastiaansen, A. P. Schenning, *J. Am. Chem. Soc*. **2014**, 136, 10585.
14. E. Steven, V. Lebedev, E. Laukhina, C. Rovira, V. Laukhin, J. S. Brooks, J. Veciana, *Mater. Horiz.* **2014**, 1, 522-528.
15. T. Fu, J. Zhu, M. Zhuo, B. Guan, J. Li, Z. Xu, Q. Li, *J. Mater. Chem. C* **2014**, 2, 4861-4866.
16. X. Yu, W. Zhang, P. Zhang, Z. Su, *Biosens. Bioelectron*. **2017**, 89, 72-84.
17. K. Hu, R. Xiong, H. Guo, R. Ma, S. Zhang, Z. L. Wang, V. V. Tsukruk, *Adv. Mater.* **2016**, 28, 3549-3556.

View Article Online
DOI: 10.1039/C7TC00686A

18. H. Cheng, J. Liu, Y. Zhao, C. Hu, Z. Zhang, N. Chen, L. Jiang, L. Qu, *Angew. Chem. Int. Edit*. **2013**, 52, 10482-10486.
19. Y. Tai, G. Lubineau, *Sci. Rep.* **2016**, 6, 19632-19640.
20. K. Saetia, J. M. Schnorr, M. M. Mannarino, S. Y. Kim, G. C. Rutledge, T. M. Swager, P. T. Hammond, *Adv. Fun. Mater.* **2016**, 24, 492-502.
21. X. Wang, Z. Xiong, Z. Liu, T. Zhang, *Adv. Mater.* **2015**, 27, 1370-1375.
22. J. Jie, W. Zhang, K. Peng, G. Yuan, C. S. Lee, S. T. Lee, *Adv. Fun. Mater.* **2008**, 18, 3251-3257.
23. M. L. Geier, J. J. McMorrow, W. Xu, J. Zhu, C. H. Kim, T. J. Marks, M. C. Hersam, *Nat. Nanotech.* **2015**, 10, 944-948.
24. C. Chen, W. Cai, M. Long, B. Zhou, Y. Wu, D. Wu, Y. Feng, *ACS Nano* **2010**, 4, 6425-6431.
25. F. Rigoni, G. Drera, S. Pagliara, A. Goldoni, L. Sangaletti, *Carbon* **2014**, 80, 356-363.
26. P. A. Russo, N. Donato, S. G. Leonardi, S. Baek, D. E. Conte, G. Neri, N. Pinna, *Angew. Chem. Int. Ed.* **2012**, 51, 11053-11057.
27. C. Chen, W. Cai, M. Long, B. Zhou, Y. Wu, D. Wu, Y. Feng, *ACS Nano* **2010**, 4, 6425-6432.
28. S. R. Ryoo, Y. K., Kim, M. H., Kim, D. H. Min, *ACS Nano* **2010**, 4, 6587-6598.
29. J. G. Simmons, *J. Appl. Phys.* **1963**, 34, 2581-2584.
30. S. Paulson, A. Helser, M. B. Nardelli, R. M. Taylor, M. Falvo, R. Superfine, S. Washburn, *Science* **2000**, 290, 1742-1744.
31. Z. Bo, Z. Wen, H. Kim, G. Lu, K. Yu, J. Chen, *Carbon* **2012**, 50, 4379-4387.
32. O. Rezvanian, C. Brown, M. A. Zikry, A. I. Kingon, J. Krim, D. L. Irving, D. W. Brenner, *J. Appl. Phys.* **2008**, 104, 024513-024518.
33. M. P. Garrett, I. N. Ivanov, R. A. Gerhardt, A. A. Puretzky, D. B. Geohegan, *Appl. Phys. Lett.* **2010**, 97, 163105-163108.
34. D. Stauffer, A. Aharony, *Introduction to Percolation Theory*, 2nd-ed. *Taylor & Francis*, London, **1992**.
35. M. D. Stoller, S. Park, Y. Zhu, J. An, R. S. Ruoff, *Nano Lett.* **2008**, 8, 3498-3502.
36. T. I. Lee, S. Lee, E. Lee, S. Sohn, Y. Lee, S. Lee, Z. L. Wang, *Adv. Mater.* **2013**, 25, 2920-2925.
37. Y. Yao, X. Chen, J. Zhu, B. Zeng, Z. Wu, X. Li, *Nanoscale Res. Lett.* **2012**, 7, 1-7.
38. A. Zahab, L. Spina, P. Poncharal, C. Marliere, *Phys. Rev. B* **2000**, 62, 10000-10004.
39. A. Kyrsting, P. M. Bendix, L. B. Oddershede, *Nano Lett.* **2013**, 13, 31-35.
40. Kenry, J. C. Yeo, J. Yu, M. Shang, K. P. Loh, C. T. Lim, *Small* **2016**, 12, 1593-1604.
41. Y. L. Tai, Z. G. Yang, *Langmuir* **2015**, 31, 13257-13264.
42. W. Yuan, G. Shi. *J. Mater. Chem. A* **2013**, 1, 10078-10091.
43. J. Feng, L. Peng, C. Wu, X. Sun, S. Hu, C. Lin, J. Dai, J. Yang, Y. Xie, *Adv. Mater.* **2012**, 24. 1969-1974.